

An aptamer SERS/RRS/Abs trimode biosensor for trace Pb²⁺ based- liquid crystal@nanosilver catalytic amplification

Yiyi Shu

Guangxi Normal University

Sha Li

Guangxi Normal University

Aihui Liang

Guangxi Normal University

Zhiliang Jiang (✉ zljjiang@mailbox.gxnu.edu.cn)

Guangxi Normal University

Research Article

Keywords: LC@AgNP catalytic amplification, AgNPs trimode indicator reaction, aptamer, inorganic pollutants

Posted Date: August 2nd, 2022

DOI: <https://doi.org/10.21203/rs.3.rs-1867949/v1>

License:   This work is licensed under a Creative Commons Attribution 4.0 International License.

[Read Full License](#)

Abstract

Liquid crystals (LCs) are a very important display material. However, the use of LC, especially LC loaded nanoparticles, as a catalyst to amplify analytical signal and coupled with specific aptamer (Apt) as recognition element to construct a highly sensitive and selective three-mode molecular spectral assay is rarely reported. In this article, five LCs such as cholesteryl benzoate (CB) were studied by molecular spectroscopy to indicate liquid crystal nanoparticles in the system, and highly catalysis and stable CB loaded-nanosilver (CB@AgNPs) sol was prepared. The slope procedure was used to study the catalysis of the five LCs and CB@AgNPs on the new indicator reaction between AgNO_3 and sodium formate (Fo) to produce silver nanoparticles (AgNPs) with a strong surface plasmon resonance absorption (Abs) peak at 450 nm, resonance Rayleigh scattering (RRS) peak at 370 nm and surface enhanced Raman scattering (SERS) peak at 1618 cm^{-1} in the presence of molecular probes. By coupling the new CB@AgNPs catalytic indicator reaction with the Apt reaction, a new CB@AgNPs catalytic amplification-SERS/RRS/Abs trimode biosensing platform was constructed for detecting for inorganic pollutants such as Pb^{2+} , Cd^{2+} , Hg^{2+} and As^{3+} .

Introduction

Liquid crystals (LC) are a kind of intermediate state polymer ordered material that combined the properties of crystal and liquid. It can have fluidity like liquid, but also has anisotropy similar to crystal [1]. Moreover, due to the elastic strain of the LC molecules, the small changes in the geomorphic surface could be further amplified to tens of microns [2]. After amplifying this small change and further converting it into a light signal observable under a polarizer, a LC sensor could be established. Compared with traditional analysis methods, it could easily detect analytes such as enzyme activity [3, 4] and trace elements [5], and had high sensitivity and did not require expensive equipment. Zhi [6] used liquid crystal (LC) trans, trans-4-(3,4-difluorophenyl)-4'-n-pentylbicyclohexyl (DP) to establish a simple and sensitive RRS energy transfer (RRS-ET) method for the determination of trace Cr^{6+} in water samples. Wang [7] realized the open-eye detection of kanamycin with LC film on glass scaffold by cross-polarizer based on the directional alignment changes of LC surface caused by Apt reaction. Wang [8] used a polarized light microscope to detect cocaine by using the conformational changes of the Apt on the water/LC interface. Verdian [9] demonstrated a novel LC based sensor platform as a labeling free and rapid detection biosensor for PCB77, which limit was $1.5 \times 10^{-5} \mu\text{g/L}$. Nanomaterials, as new materials with at least 1-100nm one-dimensional size, had been widely used in various fields. The combination of nanotechnology and LC for the determination of trace substances has been reported. The detection of amino acids, organophosphorus pesticides and enzymes by nanogold -signal amplification and nickel nanoparticles combined with LC sensor is simple and sensitive. The nanoparticles loaded in liquid crystal (LC) media has emerged an exciting field of research in recent years, because of these potentials for application and ease to control the orientation of host and self-assembled structure by external stimulus [10]. Pourmostafa [11] had found that 6CHBT doped with MgO nanoparticles will enhance the Kerr constant and birefringence effect. Huang et al [12] studied the silica nanoparticles loaded in LC that exhibit

bistable properties. As far as we know, most of the research is on the physical level and there are no reports on the CB@AgNPs catalytic amplification and its application in the detection of trace inorganic pollutants by the aptamer SERS/RRS/Abs trimode biosensing platform.

SERS is a simple and highly sensitive molecular spectroscopy technique that has been applied in many frontier fields. We knew that some small organic compounds and metal ions had small scattering cross-sections, and their SERS method had low sensitivity and selectivity. It was of great significance to couple with some selective biochemical reactions such as Apt and enzyme reactions [13]. Liu [14] established SERS detection method for determining 10 pm-1 μ M insulin-like growth factor 2 receptor protein based on Apt reaction and gold/silver nano substrate. Liang [15] detected 1.3–16 pM Pb^{2+} by SERS and RRS using the strong catalysis of the prepared AuNPs and $\text{C}_2\text{H}_2\text{O}_2\text{-HAuCl}_4$ nanoreaction. Yu [16] used AuNFs to SERS sol substrate and TMB_{OX} to the probe, and detected iodide ions by SERS method. It is different to SERS, RRS is an elastic scattering, with advantages of high sensitivity and simplicity. RRS had been used in the detection of pesticides, metal ions and other pollutants, especially combined with nanoparticles as probe. El Kurdi [17] reported that RRS signals of AuNPs could be amplified > 10 times by growing into gold nanowires (AuNPs). Patra [18] successfully synthesized polyethylene glycol block-polypropylene glycol block-polyethylene glycol (F-108) functionalized AuNPs by using RRS spectral probe to detect enzymes and labeled free sugars in serum samples. El-Kurdi [19] published the progress of chemical sensing and biosensing of gold and silver nanoparticles in RRS technology. Li [20] applied a multifunctional AuNPs probe based on anti-EGFR Apt-and anti-EGFR antibody (Ab) to EGFR-positive cancer cells. When the probe was mixed with Eca109 ESCC cancer cells, a significant increase in RRS intensity was observed. The dynamic range of the probe for Eca109 cells was $1.0 \times 10^2\text{-}5.0 \times 10^5 \text{ cell}\cdot\text{mL}^{-1}$, and the detection limit was $20 \text{ cell}\cdot\text{mL}^{-1}$. Due to the advantages and disadvantages of various analysis methods, a single detection method might have problems such as low sensitivity, poor stability and poor reproducibility. The dual mode and trimode methods could overcome these shortcomings and had attracted much attention. Based on the preparation of N-doped carbon points by microwave, Xi [21] combined with the Apt reaction of K^+ , established a fast and efficient fluorescence-RRS dual mode coupling method for the determination of trace K^+ . Yao [22] prepared a new Au nanocluster-doped covalent organic framework (AuCOF), and established a dual-mode analysis platform of SERS/RRS based on Apt-mediated COF nano-catalytic amplification signal strategy to detect ultra-trace small molecules. Huang [23] constructed a RRS/Abs dual-mode sensor using 4-heptylbenzoic acid (HPB), which could be used to determine 0.5ng/mL of oxytetracycline. Li [24] reported a new strategy of three-mode sensing based on nitrite colorimetric/fluorescence/SERS assembled by gold nanorods and azo-gold nanoparticles modulate based on Griess reaction. Wang [25] developed a new three-mode Apt detection strategy for the detection of ultra-trace As^+ based on $\text{Apt}_{\text{As}}\text{-As}^+$ reaction mediating $\text{CDAu-HAuCl}_4\text{-fructose}$ nanoreaction and the products of AuNPs as SERS/RRS/Abs trifunctional indicator nanoprobe. Compared to the reported nanocatalysts such as metal, oxide, carbon dot, COF and MOF nanoparticles, LC molecule has stable and clear structure. Further, LC forms nanoparticle catalyst by simple heating, that can couple with catalytic indicator reaction. Those advantages are attracting us to use it to amplify

trimode molecular signal to determine inorganic pollutants in environmental water and agricultural product samples.

Inorganic pollutants, such as Pb(II) is an important pollutant, with multiple sources of pollution, and it existed in water, atmosphere or biota, is extremely harmful to the human body. Pb(II) and its compounds enter the human body and have varying degrees of harmful effects on various cells and systems of the human body, damage the human hematopoietic system, nervous system and kidneys [26, 27], and caused various diseases. Therefore, it was of great significance to detect Pb²⁺ in environmental protection, agricultural product and human health. At present, there are several methods to detect Pb²⁺, such as atomic absorption spectrometry (AAS), inductively coupled plasma mass spectrometry (ICP-MS), fluorescence spectrometry (FL) and spectrophotometry [28–30]. Wang [31] adopted the colorimetric method to carry out semi-quantitative, visual and sensitive morphological analysis of Pb²⁺ in actual samples with double emission carbon points (CD), and the detection limit was 2.89 nM. Zhuang [32] combined DNA-based HCR with specific DNAzyme to establish a new magnetic-controlled electrochemical DNA biosensor for the detection of 0.1–75 nM Pb²⁺ with a detection limit of 37 pM. However the above biosensor methods were relatively complex and time-consuming. AAS and ICP-MS required pretreatment and expensive equipment. FL, colorimetry and spectrophotometry were simple to operate but low sensitivity. Based on this, a new nanosilver sol SERS/RRS/Abs biosensing platform for the determination of trace inorganic pollutants was established by combining CB@AgNPs catalytic amplification with Apt technology, which opened up a new field of LCs analysis and application.

Experimental Part

Main instruments

Hitachi F-7000 fluorescence spectrophotometer (Hitachi High-Tech Company, Japan); TU-1901 type dual-beam UV-Vis spectrophotometer (Beijing Puxi General Instrument Co., Ltd.); DXR Raman spectrometer (Thermo Fisher Scientific Company); FEI Talos 200S radio microscope (Thermo Fisher Scientific company); 16K desktop centrifuge (Zhuhai Dark Horse Medical Instrument Co., Ltd.); Ultrasonic cleaner SK3300B (Shanghai Kedao Ultrasonic Instrument Co., Ltd.); HH-1 electric heating constant temperature water bath (Shanghai Weicheng Instrument Co., Ltd.) Company); SYZ-550 type quartz sub-boiling water distiller (Jiangsu Jingbo Instrument Factory); DHG-9023A electric heating constant temperature blast drying oven (Shanghai Jinghong Experimental Equipment Co., Ltd.); FB224 automatic internal school electronic analytical balance (Shanghai Sunny Hengping Scientific Instrument Co., Ltd.); DF-101S-type heat-collecting constant temperature heating magnetic stirrer (Gongyi Yuhua Instrument Co., Ltd.); Nanoparticle size and Zeta potential analyzer (Malvern, UK); Thermofisher Talos F200s transmission electron microscope (Thermo Fisher Scientific, USA); and S-4800 field emission scanning electron microscope (Hitachi High-Technologies Corporation, Japan/Oxford Corporation, UK) were used.

Main reagents

Cholesteryl benzoate (CB), 4-octyloxybenzoic acid (OA), 4-heptylbenzoic acid (HA), trans, trans-4-(3,4-Difluorophenyl)-4'-n-pentylbicyclohexyl (DB) and trans-4-(3,4-difluorophenyl)-trans-4'-ethylbicyclohexane (DE) were obtained from Macklin Co., with LC phase temperature of 145–150°C, 101–105°C, 98°C, 44–49°C and 51–54°C respectively. A 0.049 g CB was dissolved in 10 mL ethanol/water (1:1) to obtain 0.01 mol/L CB solution. The 4-Hexyloxybenzoic acid (HB) without catalysis was obtained from Macklin. The Apt of Pb(II) was synthesized by Biological Engineering Shenggong with the sequences of GGT TGG TGT GGT TGG; C₂H₅OH (AR, Guangdong Guanghua Technology Co., Ltd.); Pb(II) nitrate (AR, Shantou Xilong Chemical Factory Co., Ltd.); Victoria Blue 4r (VB4r); AgNO₃ (AR, Guangdong Guanghua Technology Co., Ltd.); and sodium formate (Fo) were used. The reagents used were of analytical grade, and the experimental water was sub-boiling water.

Preparation of CB@AgNP: In a clean 100 mL conical flask, 5 mL 0.01 mol/L AgNO₃ was taken and added water to 25 mL, then 5 mL 0.01 mol/L CB and 20 mL saturated carbon monoxide solution were added respectively, under the condition of magnetic stirring for 2 h, to obtain 1.0 mmol/L CB@AgNP nanosol.

Preparation of AgNPs: 5 mL 0.01 mol/L AgNO₃ was taken into a clean 100 mL conical flask, then 20 mL saturated carbon monoxide solution was added into the mixture at a constant speed in the stirred state and volumed to 50 mL, finally stirred 1 h to obtain 1 mmol/L AgNPs.

Experimental procedure

A 7.4 mM (pH 4.4) NaAc-HAc (88.8 mM NaAc) buffer solution, 200 μL 0.1 mmol/L LC solution, 100 μL 100 nM Apt_{Pb}, and a certain concentration of Pb(II) solution were added into a 5 mL glass tube. After standing for 15 min, 200 μL 0.01 M AgNO₃ and 150 μL 1 M Fo were added, shaken well, the volume was fixed to 1.5 mL, and heated in 95°C water bath for 20 min. After cooling with ice water, 100 μL 1 mol/L NaCl solution and 100 μL 10 μmol/L VB4r were added to the reaction solution. The Raman spectra were obtained by scanning under the conditions of the Raman spectrometer with a light source power of 2.0 mW and a slit of 25.0 nm slit. The SERS intensity at 1618 cm⁻¹ ($I_{1618\text{cm}^{-1}}$) was measured. Without Pb²⁺, the blank SERS signal ($I_{1618\text{cm}^{-1}})_0$ was measured, then $\Delta I = I_{1618\text{cm}^{-1}} - (I_{1618\text{cm}^{-1}})_0$ was calculated. For the RRS and Abs analysis, no VB4r was added.

Results And Discussion

Analysis principle

CB belonged to cholesterol LC, and its shape showed spontaneous helical structure arrangement of layered molecules [33, 34]. When AgNPs were loaded in CB, it formed CB@AgNPs that could effectively catalyze the AgNO₃-Fonanosilver indicator reaction, and the produced AgNPs cause the increase of SERS/RRS/Abs signal. When the Apt was added before the reaction, the Apt could adsorb on the CB@AgNPs surface to inhibit its catalytic performance, so the AgNO₃-Fo reaction was difficult to carry out, and the SERS/RRS/Abs signal of the system was low. When inorganic pollutants were added, the Apt

combined with inorganic pollutants to form a stable G-tetrad structure. The CB@AgNPs recovered their catalytic activity and generated more AgNPs indicating components. The SERS/RRS/Abs signal was linearly enhanced, and a three-mode biosensing platform for the determination of inorganic pollutants such as Pb^{2+} could be constructed (Fig. 1).

Nanomaterial characterization

Transmission electron microscope of AgNPs and CB@AgNPs

The CB@AgNPs and AgNPs were prepared according to the experimental method. Then the Thermofisher Talos F200s transmission electron microscope (TEM) was used to record the image and energy spectra of the sample. As shown in (Fig. 2A), AgNP has a spherical structure, and their average particle size was about 20 nm. Compared with AgNPs, CB@AgNPs are composed of evenly distributed C, O, and Ag elements, that exhibit two peaks at 2.5 and 3 keV for Ag. It can be seen from its energy spectrum, the doping of AgNPs do not significantly change the structure of CB. And it can be clearly seen from the EDS mapping that AgNPs have been doped in CB (Fig. 2B). In addition, the TEM of AgNPs produced by the $\text{Apt}_{\text{Pb}}\text{-CB@AgNPs-Fo-AgNO}_3$ reaction were recorded (Fig. 2C). When Pb^{2+} was no addition of Pb^{2+} , the less AgNPs were formed, and its average particle size was 20 nm. When Pb^{2+} was added, a large number of AgNPs particles were generated by the reaction, and their average particle size was about 40 nm (Fig. 2D).

Molecular spectrum, Zeta potential and particle size distribution of CB, AgNPs and CB@AgNPs

RRS spectroscopy is a simple and sensitive technique for studying the scattering properties of nanoparticles. Under the condition of Volt = 350 V and excitation slit = emission slit = 5 nm, the RRS spectra of CB, AgNPs and CB@AgNPs at different temperatures can be obtained easily and quickly. Figure 3A shows that when temperature was less than 45 °C, CB exhibits the strongest RRS peak at 340 nm and there are nanoparticles at room temperature. When temperature was high than 65 °C, the strongest RRS peak changed to 370 nm. The both peak RRS values all enhanced greatly with increasing temperature, indicating that the formed CB nanoparticle numbers increased. In addition, the red-shift of strongest RRS peak was due to the size increasing. Figure 3B and C show the RRS intensity of CB@AgNPs and AgNPs were decreased with increasing temperature. Figure 3D is the UV absorption spectrum of CB. The Abs peak at 226 nm enhanced with temperature increasing that was related to the changes of CBN number and size. Figure 3E and F are the UV absorption spectrum of CB@AgNPs and AgNPs. The Abs signal value peak at 446 nm was decreased with temperature increasing.

Laser scattering was good and reliable technique to study the particle size distribution in solution because the conditions of the system were not destroyed. The particle size distribution of CB materials at different temperatures was studied by laser scattering nanoparticle analyzer. It can be clearly observed

from Fig. 3G that in a certain temperature range (35–85°C), the diameter of CB increases from 101,116,123, 154 to 171 nm when the temperature increase. This was because the CB molecules gradually were aggregate into nanoparticles with larger size as the temperature increases. Figure 3J shows that the surface of CBN material is negatively charged, and the Zeta potential is -0.138 mV, indicated it was of good stability. The particle size distribution of CB@AgNPs and AgNPs materials at different temperatures was studied by laser scattering nanoparticle analyzer. It can be clearly observed from Fig. 3H and I that in a certain temperature range (35–85°C), the diameter of CB@AgNPs and AgNPs decreases when the temperature increase.

Using nanosilver as SERS base, we studied the Raman spectrum of CB solution. The results show that there is no obvious characteristic peak. After that, 0.1m NaCl solution was added as sensitizer, but there was still no obvious characteristic peak on the spectrum. Therefore, a small amount of solid CB powder was dried by rectangular glass plate, then the other glass sheet was rolled, the CB powder was dispersed, and then placed in a Raman measurement instrument to obtain CB normal Raman spectra. The normal Raman spectra of CB solid (Fig. 3K) show 8 peaks, of which 865 cm^{-1} is ring "respiration", 1003 cm^{-1} is the triangular ring "breathing"; 1275 cm^{-1} is the ring vibration of a para-disubstituted benzene ring; 1445 cm^{-1} is a ring stretch; 1601 cm^{-1} is caused by the expanded ring peak (double peak) of benzene derivatives; $854, 1154$ and 1284 cm^{-1} are attributed to ring vibration of the para-disubstituted benzene ring; 1608 cm^{-1} is caused by the expanded ring peak (double peak) of benzene derivatives; 1713 cm^{-1} is an extension of the C-O bond; 2864 cm^{-1} and 3075 cm^{-1} were attributed to CH_3 stretching and aromatic C-H stretching, respectively. Using nanosilver as SERS base, and 0.1m NaCl solution was added as sensitizer, we studied the Raman spectrum of CB@AgNPs solution. The results (Fig. 3K) show that 7 peaks, of which 436 cm^{-1} and 679 cm^{-1} are skeletal bending, which 878 cm^{-1} is ring "respiration", 1485 cm^{-1} is a ring stretch; 1615 cm^{-1} is caused by the expanded ring peak (double peak) of benzene derivatives; 2933 cm^{-1} is attributed to aromatic C-H stretching and 3441 cm^{-1} is attributed to aromatic O-H stretching.

Figure 3L shows the infrared spectrum of CB, in which the characteristic peaks at 994 cm^{-1} are caused by the out-of-plane curvature of C-H, and 1109 cm^{-1} is the C-O bond caused by expansion and contraction; 1271 cm^{-1} is an in-plane flexion caused by a para-substituted phenyl group; $1369, 1449$ and 1711 cm^{-1} are extensions of C-O bonds; 2341 and 2361 cm^{-1} are vibration peaks caused by triple bonds and cumulative double bonds; 2936 cm^{-1} is the stretching vibration peak caused by CH. Figure 3L shows the infrared spectrum of CB@AgNPs, in which the characteristic peaks at 853 cm^{-1} is caused by the out-of-plane curvature of C-H; 1337 is extensions of C-O bonds; 3226 and 3449 cm^{-1} are the stretching vibration peak caused by CH.

To test the stability of AgNPs and CB@AgNPs, their stability in NaCl and over time were investigated respectively. $200\text{ }\mu\text{L}$ 1 mmol/L AgNPs and CB@AgNPs in a 10 mL plug calibrated tube, Different volumes of 1 mol/L NaCl solution were added, and the volume was fixed to 1.5 mL . After the mixture was evenly

mixed, RRS signal was measured (Figure S1A, S1B). Figure S1A shows that with the increase of days, the RRS signal values of AgNPs and CB@AgNPs were in a stable state. In addition, the stability of these catalytic materials was investigated in different concentrations of NaCl solutions, it was also found that the AgNPs materials were unstable in NaCl solutions with different concentrations, and the signal value would rise first and then increased slightly, which might be caused by AgNPs aggregation in salt solutions. The signal values of CB@AgNPs in the low salt solution were very stable. With the increase of NaCl concentration, the signal values increased slightly, which might be caused by AgNPs aggregation in the solution. The results showed that CB@AgNPs was relatively stable in salt solution and for a long time, while AgNPs had poor stability and tended to aggregate in salt solution. So when AgNPs were mixed with CB, it could be uniformly loaded in CB, which had a greater improvement in the stability of the salt than AgNPs.

SERS spectra of nanocatalytic system

Under experimental conditions, AgNO_3 was reduced to AgNPs by Fo slowly, and fewer AgNPs were generated in the system. When the CB@AgNPs/AgNPs/LC catalysts were added to the system, the reaction of the AgNPs were significantly accelerated, and the generated AgNPs were not only the indicator component but also the sol substrate. When VB4r was added as probe, a strong SERS peak appeared at 1618 cm^{-1} . When Apt_{Pb} was present, it was adsorbed to the surface of CB@AgNPs catalyst, the catalytic activity decreased, and the generated AgNPs decreased, which led to the decrease of SERS signal of the system. When Pb^{2+} was added, Apt_{Pb} combined with Pb^{2+} to generate a stable G-tetrad structure, the catalytic activity of the CB@AgNPs were restored, the generated AgNPs increased, and SERS signal was linearly enhanced. Within a certain concentration range, the SERS signal of the system was gradually enhanced with the increase of the concentration of the substance to be measured, and the SERS peak of the system at 1615 cm^{-1} increased linearly (Fig. 4A). The other inorganic pollutants to be measured, namely As^{3+} , Cd^{2+} and Hg^{2+} , were less sensitive than Pb^{2+} (Fig. 4C, 4D, 4E). From the slope of the linear curve of CB@AgNPs/AgNPs/LC concentration and SERS peak, we could know that the slope of CB@AgNPs system was the largest and its catalytic effect was the strongest (Fig. 4A, Figure S2A-E).

RRS spectra of catalytic amplification system

RRS was no addition of VB4r, and it is more simply than the SERS. Under experimental conditions, the AgNPs generated by $\text{Apt}_{\text{Pb}}\text{-CB@AgNPs-Fo-AgNO}_3\text{-Pb}^{2+}$ system had a strong RRS peak at 370 nm. Within a certain concentration range, the RRS signal of the system was gradually enhanced with the increase of the Pb^{2+} concentration (Fig. 5A), based on which a new RRS method for detecting Pb^{2+} could be established. In addition, the RRS spectra of $\text{Apt-CB@AgNPs-Fo-AgNO}_3\text{-As}^{3+}/\text{Cd}^{2+}/\text{Hg}^{2+}$ show in Fig. 5B-D. The $\text{Apt}_{\text{Pb}}\text{-AgNPs/LC-Fo-AgNO}_3\text{-Pb}^{2+}$ system also has a RRS peak (Figure S3A-F).

Abs spectra of catalytic amplification system

Under the experimental conditions, the AgNPs produced by the $\text{Apt}_{\text{Pb}}\text{-CB@AgNPs-Fo-AgNO}_3\text{-Pb}^{2+}$ system had an absorption peak at 450 nm, which was corresponded to the surface plasmon resonance

absorption peak of AgNPs. Within a certain concentration range, as the concentration of Pb^{2+} increased, the absorbance of the system gradually increased, and an absorption peak appeared at 450 nm (Fig. 6A). Similarly, the AgNPs/CB system has an absorption peak at 430 nm, the AgNPs, OA and HA systems have an absorption peak at 450 nm (Fig. 6B, 6C). In addition, the DB and DE nanocatalytic analytical systems have an absorption peak at 440 nm (Figure S4A-F). In which, the CB@AgNPs catalytic analytical system was most sensitive.

CB@AgNPs and LC catalytic mechanism

Under the catalysis of CB@AgNPs, AgNO_3 was reduced by Fo to produce AgNPs. Within a certain concentration range, as the concentration of the catalyst increased, the catalytic ability increased, and the amount of AgNPs generated by catalysis increased, which had a strong RRS peak at 370 nm. Table S1 shows that the slope of the working curve of the CB@AgNPs RRS system was 7 times that of CB and 2 times that of AgNPs respectively, it can be seen that the slope of the CB@AgNPs system is the largest, and most AgNPs are generated in the system. When Apt_{Pb} was added to the system, it could be adsorbed on the surface of the catalyst due to static electricity and molecular forces, and inhibited its catalytic activity. With the increased of Apt_{Pb} concentration, the concentration of free catalyst in the system decreased, and the catalytic activity weakened, thus the AgNPs generated in the system decreased, and the RRS signal of the system weakened (Table S1).

Because the hydrogen bond association force in the cholesterol molecule is so strong that when the solid reaches its melting point, the solid directly became an isotropic liquid, which means that cholesterol did not have an LC phase, and CB had an LC phase. The ring system in the molecule is another important factor that determines whether the molecule has an LC phase. Molecules with aromatic rings do not necessarily have an LC phase, but molecules with an LC phase almost all have more than one aromatic ring. Like the five LC molecules and CB@AgNPs used in this experiment, when the solid melts into a liquid, the aromatic ring maintain the intermolecular relationship. The short-range attractive force prevents the molecule from turning into an isotropic liquid immediately. Common ring systems include saturated six rings and unsaturated benzene rings, or a combination of the two. The electrons in the saturated six-membered ring were σ electrons, which are not conjugated to each other, while the electrons in the benzene ring are π electrons, which have a conjugation effect. Conjugation of electrons have an important influence on the properties of LCs, especially the π electrons in the benzene ring help to promote electron transfer in redox reactions. The study finds that these five LCs and CB@AgNPs materials can catalyze the reduction of AgNO_3 by Fo to generate AgNPs. Among the five types of LC and CB@AgNPs, the slope of the linear relationship between CB@AgNPs concentration and SERS/RRS/Abs is the largest, and it has the strongest catalytic effect on the AgNO_3 -Fo system, this is very related to molecular structure of CB (Fig. 7) with the most π electrons and without electron absorbing base F, and the higher LC phase temperature of 145–150°C that is easy to form CB nanoparticles. Nanoparticles such as metal nanozymes, semiconductor nanozymes, carbon dot nanozymes, metal organic framework nanozymes, and covalent organic framework nanozymes are rich in surface electrons, which are the driving force for promoting electron transfer in some redox reactions. The formate reduction of AgNO_3

can slowly generate AgNPs and CO₂. These five small molecules of LC and CB@AgNPs can be arranged and assembled into rod-shaped nanoparticles in an aqueous solution at 95 °C, and their surface is rich in surface electrons. Ag⁺ and HCOO⁻ can be adsorbed on the surface of LC and CB@AgNPs nanoparticles. This nano surface electron can accelerate the redox electron transfer between formic acid and silver ions, accelerate the formation of AgNPs, and show a strong catalytic effect (Fig. 7).

Optimization of analysis conditions

According to the experimental method, the SERS analysis system conditions were examined. When the experimental conditions were 0.667 nmol/L Apt_{Pb} (Figure S5A), 73.98 μmol/L NaAc-HAc (Figure S5B), 1.33 mmol/L AgNO₃ (Figure S5C), 0.1 mol/L Fo (Figure S5D), reaction temperature was 95 °C (Figure S5E), reaction time was 20 min (Figure S5F), 1.33 μmol/L CB@AgNPs (Figure S5G), standing time was 15min (Figure S5H), 0.67 μmol/L VB4r (Figure S5I), 0.067 mol/L NaCl solution (Figure S5J), the SERS signal of the analysis system was the largest, so these conditions were selected as the SERS experimental conditions.

According to the experimental method, the RRS analysis system conditions were considered. When the experimental conditions were 0.667 nmol/L Apt_{Pb} (Figure S6A), 73.98 μmol/L NaAc-HAc (Figure S6B), 1 mmol/L AgNO₃ (Figure S6C), 0.1 mol/L Fo (Figure S6D), reaction temperature was 85 °C (Figure S6E), reaction time was 15 min (Figure S6F), 1.33 μmol/L CB@AgNPs (Figure S6G), standing time was 15min (Figure S6H), the ΔI of the analysis system was the largest, so the above conditions were selected for use. The conditions of the Abs method were the same as those of the RRS method.

3.8. Working curve

Under the optimal experimental conditions, the different concentrations of Pb²⁺ were plot its corresponding ΔI/ΔA to obtain the working curve, it could be seen from the Table S2 and 3 show that the slope of the working curve of the Apt-CB@AgNPs system was 5 times that of CB and 1.5 times that of AgNPs respectively, indicating that it was the most sensitive. The linear equation was $\Delta I_{1618\text{cm}^{-1}} = 76201C + 414.6$, and the linear range was 4.47×10^{-3} -0.201 nmol/L. Although RRS/Abs had a short reaction time and low cost, its sensitivity was not as good as SERS (Table S2). In addition, other inorganic pollutants such as As³⁺, Cd²⁺ and the Hg²⁺ can be also determined by CB@AgNPs nanocatalytic-SERS/RRS assay platform (Table S3). Comparing with the reported methods for measuring lead ions (Table S4), this method is a more sensitive molecular spectral method.

Influence of interfering ions

According to the experimental method, the interference of coexisting ions on the Apt_{Pb}-CB@AgNPs-Fo-AgNO₃-Pb²⁺ SERS determination of 0.1 nmol/L Pb²⁺ was investigated. The experimental results showed that the relative error is within ± 10%, 1000 times Mg²⁺, Ba²⁺, Mn²⁺, Cr⁶⁺, Fe²⁺, Cr³⁺, Ca²⁺, BSA; 500 times

Zn^{2+} , NH_4^+ , Co^{2+} , serum protein, ascorbic acid, Al^{3+} ; 100 times Fe^{3+} , Hg^{2+} , Cu^{2+} , NO_2^- , HSA, PO_4^{3-} do not interfere with the measurement (see Table S5). This method has good selectivity.

Sample determination

Tap water and mineral water were 100mL each, and a water sample was taken from pond water of Yanshan Campus of Guangxi Normal University and wastewater of Bokang Building Laboratory of Guangxi Normal University. The sample pretreatment: orange peels and preserved eggs were all purchased from local supermarkets. Different orange peels and preserved eggs were respectively weighed and cut into small pieces and dried 10h in an oven at 105°C. The dried sample was ground with an agate mortar. 2.0 g (accurate to 0.1 mg) of sample was weighed and put in a 25 mL conical flask with 10 mL mixed acid of HNO_3 and HClO_4 ($V_1:V_2 = 4:1$) and placed overnight about 12h. The flask was placed on a power adjustable heating plate to digest until the white smoke appeared. When the solution became colorless and transparent or slightly yellow, it took down and cooled. Then the volume was adjusted to 10 mL^[41]. Finally, 100 μL samples were collected after filtration with 0.45 μm microporous membrane. According to the experimental method, the Pb^{2+} was measured, and the known concentration of $\text{Pb}(\text{II})$ was added. The detection results were shown in Table S6. The content of Pb^{2+} in water samples was 0.033–0.3310 nmol/L, and the content of Pb^{2+} in food was 4.986–16.653 ng/g. The relative standard deviation (RSD) was 1.3–7.1%, and the recovery rate was 92.53–109.4%, showed good recovery and reproducibility.

Conclusion

The CB@AgNPs , AgNPs and LCs were characterized by Zeta nanoparticle analyzer and molecular spectroscopy. The results showed that the catalytic activity of LCs was evaluated by the slope procedure using molecular spectroscopy. It was found that CB@AgNPs had the strongest catalytic effect on the nanoreaction of $\text{AgNO}_3\text{-Fo}$ due to its rich surface electrons on the CB@AgNPs nanoparticles. This new and highly sensitive catalytic amplification indicator reaction were combined with highly selective Apt reaction, with SERS/RRS/Abs molecular spectral technology, a new three-mode biosensing assay platform for the determination of Pb^{2+} was established. The SERS linear response range was 4.47×10^{-3} to 0.201 nmol/L, and the detection limit was as low as 3×10^{-3} nmol/L. The method had also been successfully applied to determine trace $\text{Pb}(\text{II})$ in food and water samples. Similarly, the apt sensor can also be applied to other inorganic pollutants detection in environmental samples, which has great potential in biochemical analysis.

Declarations

CRedit authorship contribution statement

Yiyi Shu: Software, Visualization, Writing -- original draft, Investigation, Formal analysis. **and Aihui Liang and ShaLi:** Software, Visualization, Writing – original draft, Investigation, Formal analysis. **Zhiliang Jiang:**

Software, Visualization, Writing – review & editing, Software, Methodology, Validation, Formal analysis, Conceptualization, Supervision.

Declaration of Competing Interest

The authors declare that they have no known competing financial interests or personal relationships that could have appeared to influence the work reported in this paper.

Data and Code Availability Statement

All the references cited are available.

Funding

This article was funded by the National Natural Science Foundation of China (21767004).

Acknowledgements

This article was funded by the National Natural Science Foundation of China (21767004).

References

1. Bai Y, Abbott NL (2010) Recent advances in colloidal and interfacial phenomena involving liquid crystals, *Langmuir*. 27: 5719–5738, <https://pubs.acs.org/doi/10.1021/la103301d>.
2. Koenig JGM, Ong R, Cortes AD, Moreno-Razo JA, Pablo JJ, Abbott NL (2009) Single nanoparticle tracking reveals influence of chemical functionality of nanoparticles on local ordering of liquid crystals and nanoparticle diffusion coefficients, *Nano letters*. 7:2794–2801, <https://pubs.acs.org/doi/10.1021/nl901498d>.
3. Chawla M, Kumar R, Siril PF (2016) High catalytic activities of palladium nanowires synthesized using liquid crystal templating approach, *Journal of Molecular Catalysis A: Chemical*. 423:126–134, <https://doi.org/10.1016/j.molcata.2016.06.014>.
4. Kato T, Yoshio M, Ichikawa T, Soberats B, Ohno H, Funahashi M (2017) Transport of ions and electrons in nanostructured liquid crystals, *Nature Reviews Materials*. 4:17001, <https://doi.org/10.1038/natrevmats.2017.1>.
5. Rouhbakhsh Z, Verdian A, Rajabzadeh G (2020) Design of a liquid crystal-based aptasensing platform for ultrasensitive detection of tetracycline, *Talanta*. 206:120246, <https://doi.org/10.1016/j.talanta.2019.120246>.
6. Zhi SF, Li CN, Jiang ZL (2022) A novel liquid crystal resonance Rayleigh scattering spectral probe for determination of trace Cr⁶⁺, *Spectrochimica Acta Part A: Molecular and Biomolecular Spectroscopy*. 278:121306, <https://doi.org/10.1016/j.saa.2022.121306>.
7. Wang Y, Wang B, Shen J, Xiong X, Deng S (2017) Aptamer based bare eye detection of kanamycin by using a liquid crystal film on a glass support, *Microchimica Acta*. 10:3765–3771,

<https://doi.org/10.1007/s00604-017-2405-y>.

8. Wang S, Zhang G, Chen Q, Zhou J, Wu Z (2019) Sensing of cocaine using polarized optical microscopy by exploiting the conformational changes of an aptamer at the water/liquid crystal interface. *Microchimica Acta*, 11:1–7, <https://doi.org/10.1007/s00604-019-3855-1>.
9. Verdian A, Rouhbakhsh Z, Fooladi E (2021) An ultrasensitive platform for PCB77 detection: New strategy for liquid crystal-based aptasensor fabrication, *Journal of Hazardous Materials*. 402:123531, <https://doi.org/10.1016/j.jhazmat.2020.123531>.
10. Pourmostafaab D, Tajalliab H, Vahediab A, Milanchianc K (2020) Electro-optical Kerr effect of 6CHBT liquid crystal doped with MgO nanoparticles in different concentration, *Optical Materials*. 107:110061, <https://doi.org/10.1016/j.optmat.2020.110061>.
11. Budaszewski D, Chychłowski M, Budaszewska A, Bartosewicz B, Jankiewicz B, Woliński TR (2019) Enhanced efficiency of electric field tunability in photonic liquid crystal fibers doped with gold nanoparticles, *Optics Express*. 27 (10):14260, <https://doi.org/10.1364/OE.27.014260>.
12. Huang CY, Lai CC, Tseng YH, Yang YT, Tien CJ, Lo KY (2008) Silica-nanoparticle-doped nematic display with multistable and dynamic modes, *Applied Physics Letters*. 92 (22):011704, <https://doi.org/10.1063/1.2938880>.
13. Sun Y, Li Z, Huang X, Zhang D, Zou X, Shi J, Zhai X, Jiang C, Wei X, Liu T (2019) A nitrile-mediated aptasensor for optical anti-interference detection of acetamiprid in apple juice by surface-enhanced Raman scattering, *Biosensors and Bioelectronics*. 145:111672, <https://doi.org/10.1016/j.bios.2019.111672>.
14. Liu Y, Tian H, Chen X, Liu W, Xia K, Huang J, Chapelle ML, Huang G, Zhang Y, Fu W (2020) Indirect surface-enhanced Raman scattering assay of insulin-like growth factor 2 receptor protein by combining the aptamer modified gold substrate and silver nanoprobe, *Microchimica Acta*. 187:1–9, <https://doi.org/10.1007/s00604-020-4126-x>.
15. Liang AH, Zhang R, Huang XF, Jiang ZL (2022) A new Fe/N doped carbon dot nanocatalytic amplification-aptamer SERS/RRS/Abs trimode assay platform for ultratrace Pb²⁺, *Spectrochimica Acta Part A: Molecular and Biomolecular Spectroscopy*. 272:121008, <https://doi.org/10.1016/j.saa.2022.121008>.
16. Yu FX, Jiang ZL (2021) A new gold nanoflower sol SERS method for trace iodine ion based on catalytic amplification, *Spectrochimica Acta Part A: Molecular and Biomolecular Spectroscopy*. 255:119738, <https://doi.org/10.1016/j.saa.2021.119738>.
17. Kurdi ER, Patra D (2017) Amplification of resonance Rayleigh scattering of gold nanoparticles by tweaking into nanowires: Bio-sensing of α -tocopherol by enhanced resonance Rayleigh scattering of curcumin capped gold nanowires through non-covalent interaction, *Talanta*. 168:82–90, <https://doi.org/10.1016/j.talanta.2017.03.021>.
18. Kurdi ER, Patra D (2018) Tuning the surface of Au nanoparticles using poly (ethylene glycol)-block-poly (propylene glycol)-block-poly (ethylene glycol): enzyme free and label free sugar sensing in

- serum samples using resonance Rayleigh scattering spectroscopy, *Physical Chemistry Chemical Physics*. 20:9616–9629, <https://doi.org/10.1039/c8cp01147h>.
19. Kurdi ER, Patra D (2019) Gold and silver nanoparticles in resonance Rayleigh scattering techniques for chemical sensing and biosensing: a review, *Microchimica Acta*. 186:1–18, <https://doi.org/10.1007/s00604-019-3755-4>.
 20. Li J, Wang S, Kang W, Li N, Guo F, Chang H, Wei W (2021) Multifunctional gold nanoparticle based selective detection of esophageal squamous cell carcinoma cells using resonance Rayleigh scattering assay, *Microchemical Journal*. 163:105905, <https://doi.org/10.1016/j.microc.2020.105905>.
 21. Wang X, Jiang X, Zhang Z, Li J, Liang A, Jiang Z (2019) A fluorescence and resonance Rayleigh scattering di-model probe was developed for trace K⁺ coupled N-doped carbon dot and aptamer, *Journal of Luminescence*. 214:116559, <https://doi.org/10.1016/j.jlumin.2019.116559>.
 22. Yao DM, Li CN, Wang HL, Wen GQ, Liang AH, Jiang ZL (2020) A new dual-mode SERS and RRS aptasensor for detecting trace organic molecules based on gold nanocluster-doped covalent-organic framework catalyst, *Sensors and Actuators B: Chemical*. 319:128308, <https://doi.org/10.1016/j.snb.2020.128308>.
 23. Huang HB, Li JJ, Pan SQ, Wang HL, Liang AH, Jiang ZL (2021) A novel small molecular liquid crystal catalytic amplification-nanogold SPR aptamer absorption assay for trace oxytetracycline, *Talanta*. 233:122528, <https://doi.org/10.1016/j.talanta.2021.122528>.
 24. Li D, Ma Y, Duan H, Deng W, Li D (2018) Griess reaction-based paper strip for colorimetric/fluorescent/SERS triple sensing of nitrite, *Biosensors and Bioelectronics*. 99:389–398, <https://doi.org/10.1016/j.bios.2017.08.008>.
 25. Wang HL, Zhang ZH, Chen C, Liang AH, Jiang ZL (2021) Fullerene carbon dot catalytic amplification-aptamer assay platform for ultratrace As³⁺ utilizing SERS/RRS/Abs trifunctional Au nanoprobe, *Journal of Hazardous Materials*. 403:123633, <https://doi.org/10.1016/j.jhazmat.2020.123633>.
 26. Marbella L, Serli-Mitasev B, Basu P (2009) Development of a fluorescent Pb²⁺ sensor, *Angewandte Chemie*. 121:4056–8, <https://onlinelibrary.wiley.com/doi/10.1002/anie.200806297>.
 27. Chen K, Lee C, Rick J, Wang S, Liu C, Hwang B (2012) Fabrication and application of amperometric glucose biosensor based on a novel PtPd bimetallic nanoparticle decorated multi-walled carbon nanotube catalyst, *Biosensors and Bioelectronics*. 33:75–81, <https://doi.org/10.1016/j.bios.2011.12.020>.
 28. Tang M, Wen GQ, Luo Y, Kang C, Liang AH, Jiang ZL (2015) A label-free DNAzyme-cleaving fluorescence method for the determination of trace Pb²⁺ based on catalysis of AuPd nanoalloy on the reduction of rhodamine 6G, *Journal of Luminescence*. 30:296–302, <https://doi.org/10.1002/bio.2728>.
 29. Hai H, Yang F, Li J (2013) Highly sensitive electrochemiluminescence “turn-on” aptamer sensor for lead (II) ion based on the formation of a G-quadruplex on a graphene and gold nanoparticles modified electrode, *Microchimica Acta*. 45:893–901, <https://doi.org/10.1007/s00604-014-1177-x>.

30. Yu Z, Zhou W, Han J, Li Y, Fan L, Li X (2016) Na⁺-induced conformational change of Pb²⁺-stabilized G-quadruplex and its influence on Pb²⁺ detection, *Analytical Chemistry*. 88:9375–9380, <https://pubs.acs.org/doi/full/10.1021/acs.analchem.6b02466>.
31. Wang H, Yang L, Chu S, Liu B, Zhang Q, Zou L, Yu S, Jiang C (2019) Semiquantitative visual detection of lead ions with a smartphone via a colorimetric paper-based analytical device, *Analytical Chemistry*. 91:9292–9299, <https://pubs.acs.org/doi/10.1021/acs.analchem.9b02297>.
32. Zhuang J, Fu L, Xu M, Zhou Q, Chen G, Tang D (2013) DNAzyme-based magneto-controlled electronic switch for picomolar detection of lead (II) coupling with DNA-based hybridization chain reaction, *Biosensors and Bioelectronics*. 45:52–57, <https://doi.org/10.1016/j.bios.2013.01.039>.
33. Pathinti RS, Gollapelli B, Jakka SK, Vallamkondu J (2021) Green synthesized TiO₂ nanoparticles dispersed cholesteric liquid crystal systems for enhanced Optical and Dielectric Properties, *Journal of Molecular Liquids*. 20:116877, <https://doi.org/10.1016/j.molliq.2021.116877>.
34. Yip W, Welch C, Mehl GH, Wilkinson TD (2020) A cholesteric liquid crystal device having stable uniform lying helix structure, *Journal of Molecular Liquids*. 299:112141, <https://doi.org/10.1016/j.molliq.2019.112141>.
35. B Zhang, C Wei (2018) Highly sensitive and selective detection of Pb²⁺ using a turn-on fluorescent aptamer DNA silver nanoclusters sensor, *Talanta*. 182:125–130, <https://doi.org/10.1016/j.talanta.2018.01.061>.
36. Deng H, Huang L, Chai Y, Yuan R, Yuan Y (2019) Ultrasensitive photoelectrochemical detection of multiple metal ions based on wavelength-resolved dual-signal output triggered by click reaction, *Analytical Chemistry*. 91:2861–2868, <https://pubs.acs.org/doi/10.1021/acs.analchem.8b04831>.
37. H Wang, L Ma, B Fang, F Tan, Y Cao, Y Zhao, X Hu (2018) Visual detection of Pb²⁺ using strip biosensor based on PS2M aptamer and sensitivity enhancement probe, *Sensors and Actuators B: Chemical*. 261:307–315, <https://doi.org/10.1016/j.snb.2018.01.167>.
38. Guerrini L, Alvarez-Puebla RA (2019) Multiplex SERS Chemosensing of Metal Ions via DNA-Mediated Recognition, *Analytical Chemistry*. 91:11778–11784, <https://pubs.acs.org/doi/10.1021/acs.analchem.9b02385>.
39. Wang HL, Liang AH, Wen GQ, Jiang ZL (2021) A simple SPR absorption method for ultratrace Pb²⁺ based on DNAzyme-COFPd nanocatalysis of Ni-P alloy reaction, *Sensors and Actuators B: Chemical*, 330129381, <https://doi.org/10.1016/j.snb.2020.129381>.
40. Feng D, Li P, Chen Q, Han H (2020) Electrochemiluminescence aptasensor for multiple determination of Hg²⁺ and Pb²⁺ ions by using the MIL-53 (Al)@ CdTe-PEI modified electrode, *Analytica Chimica Acta*. 1100232–9, <https://doi.org/10.1016/j.aca.2019.11.069>.

Figures

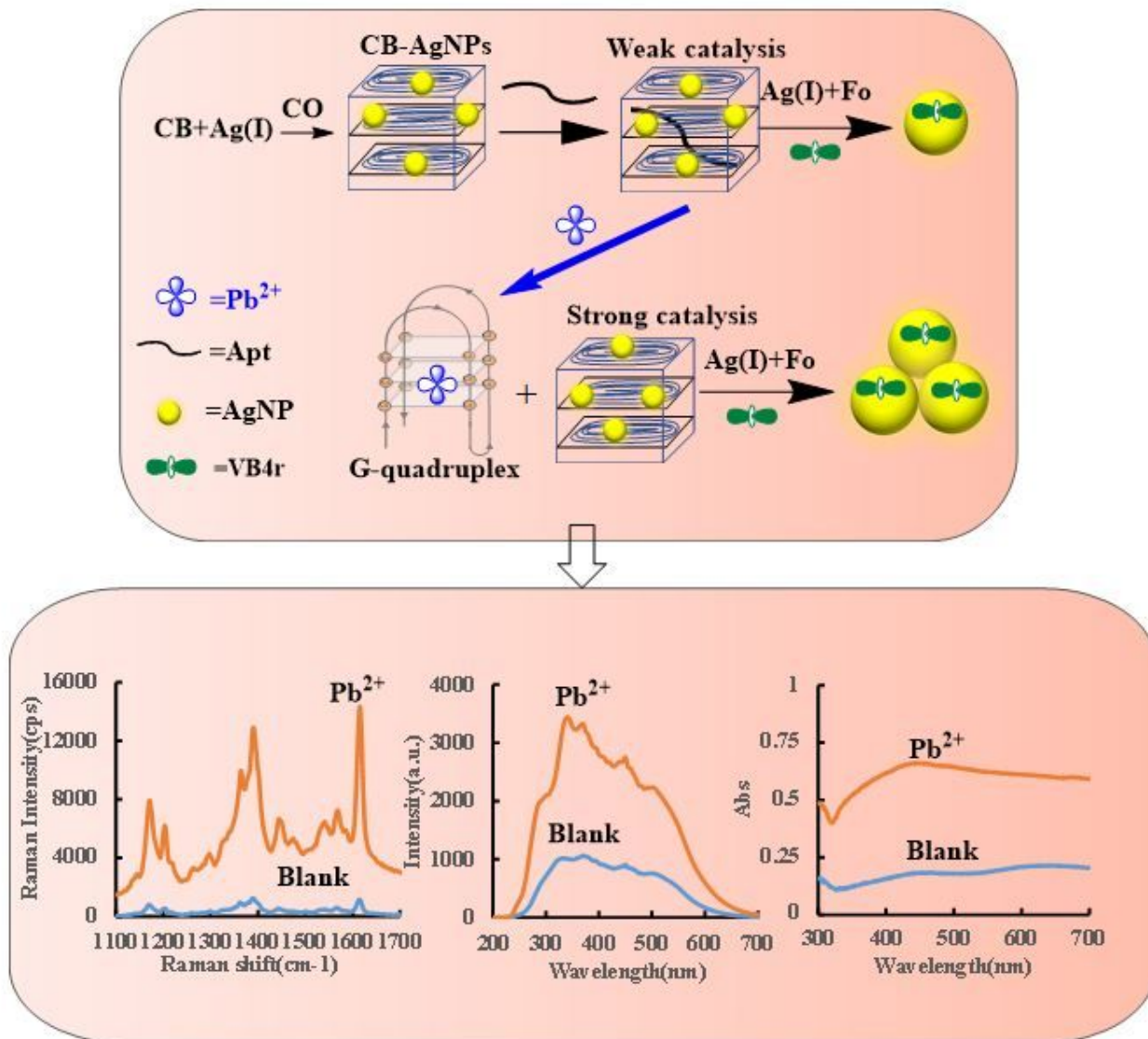


Figure 1

SERS/RRS/Abs trimode detection of inorganic pollutant Pb^{2+} coupled CB@AgNPs catalysis amplification with the Apt

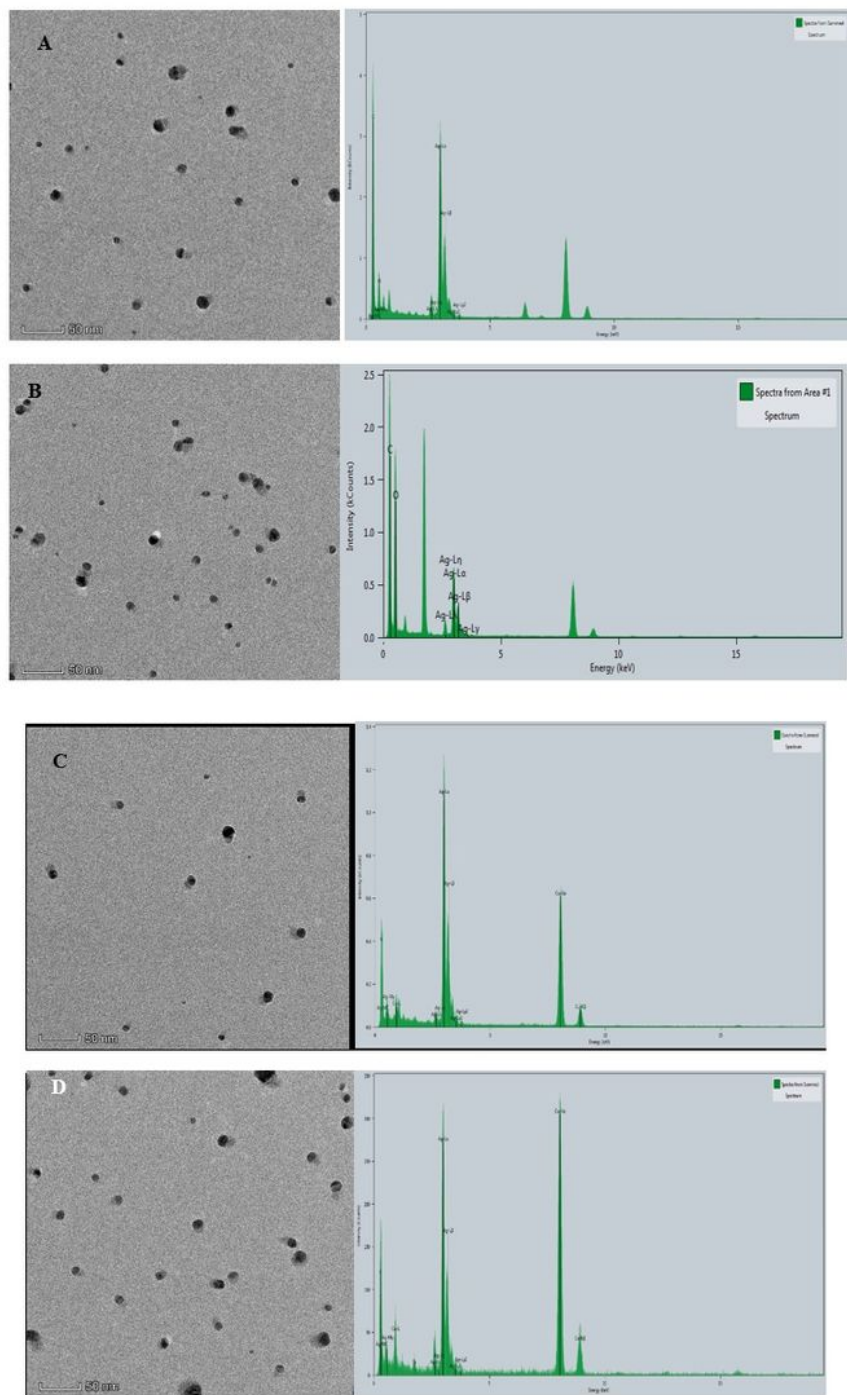


Figure 2

Transmission electron microscope of AgNPs and CB@AgNPs

A: CB@AgNPs; B; AgNPs; C: 0.667 nmol/L Apt_{Pb} +73.98 μmol/L NaAc-HAc+1.33 μmol/L CB +1.33 mmol/L AgNO₃+0.1 mol/L Fo; D: C+0.133nmol/L Pb²⁺.

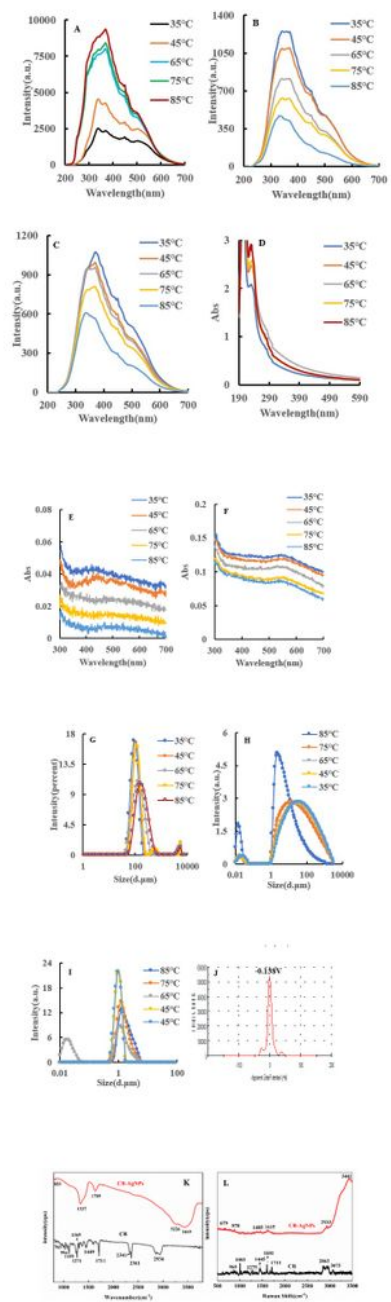


Figure 3

Molecular spectroscopy, particle size analysis and surface charge analysis of small molecule CB/CB@AgNPs/AgNPs.

A/B/C: Represents the RRS spectra of 0.01mmol/L CB/CB@AgNPs/AgNPs at different temperatures; D/E/F: Abs spectra of 0.01mmol/L CB/CB@AgNPs/AgNPs at different temperatures; G/H/I: Particle size distribution of 0.01mmol/L CB/CB@AgNPs/AgNPs at different temperatures; J: 0.01mmol/L CB (zeta potential = -0.138mV); K: Normal Raman spectrum (CB/CB@AgNPs); L: FITR spectrum (CB/CB@AgNPs).

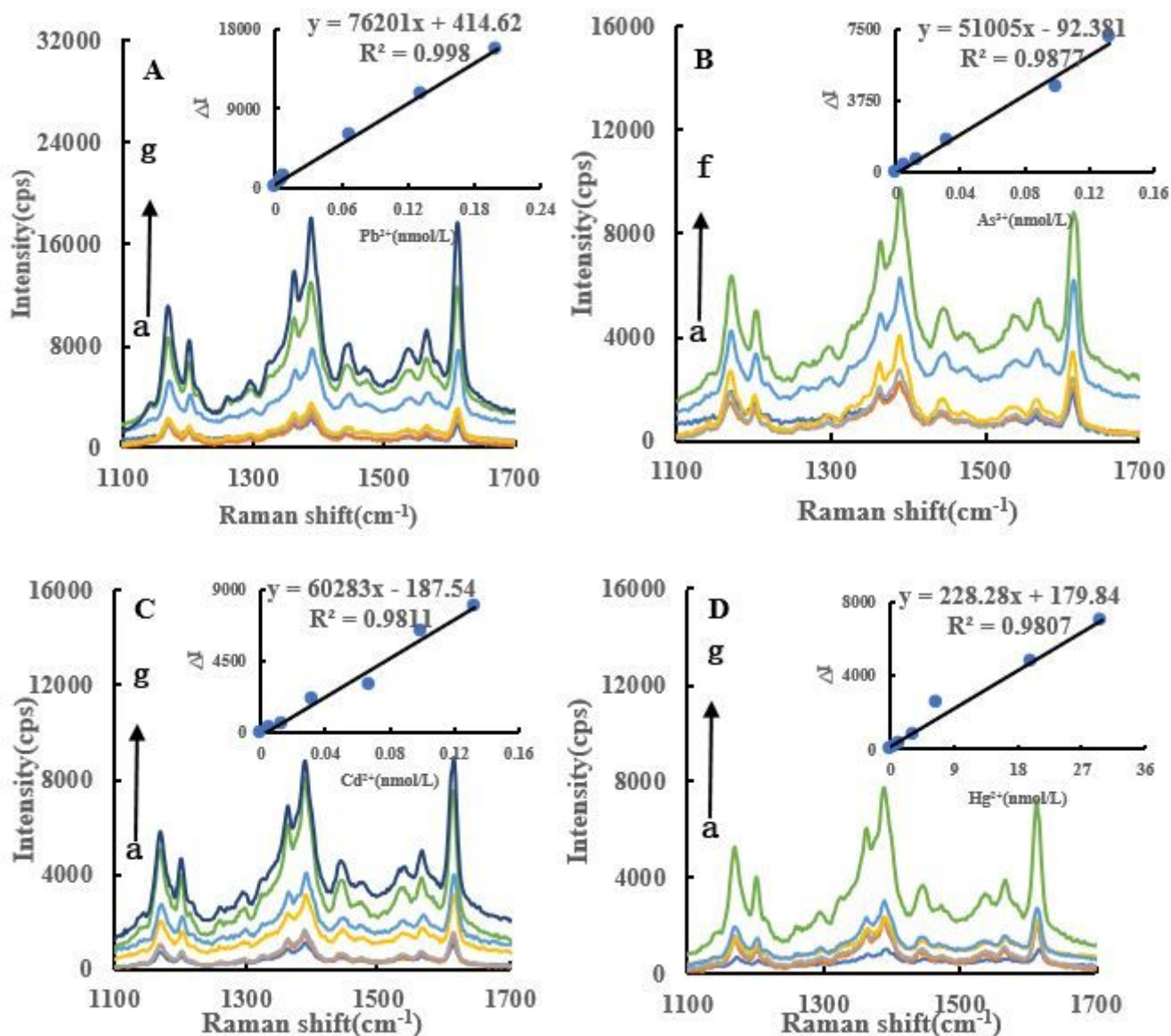


Figure 4

SERS spectra of CB@AgNPs -Fo-AgNO₃-Apt-inorganic pollutants system

A: Apt_{Pb}+NaAc-HAc+CB@AgNPs+AgNO₃+Fo+VB4r+NaCl, a to g represent 0, 4.47×10⁻³, 6.7×10⁻³, 8.94×10⁻³, 6.7×10⁻², 0.133 nmol/L Pb²⁺ and 0.201 nmol/L Pb²⁺ respectively. H: Apt_{As}+NaAc-HAc+CB@AgNPs+AgNO₃+Fo+VB4r+NaCl, a to f represent 0, 6.7×10⁻³, 1.33×10⁻², 3.3×10⁻², 0.1 and 0.133 nmol/L As³⁺ respectively. I: Apt_{Cd}+NaAc-HAc+ CB@AgNPs + AgNO₃+Fo+VB4r+NaCl a to g represent 0, 6.7×10⁻³,

1.33×10^{-2} , 6.7×10^{-2} , 3.3×10^{-2} , 0.1 and 0.133 nmol/L Cd^{2+} respectively. J: $\text{Apt}_{\text{Hg}} + \text{NaAc-HAc} + \text{CB@AgNPs} + \text{AgNO}_3 + \text{Fo} + \text{VB4r} + \text{NaCl}$, a to g represent 0, 0.67, 1.33, 3.3, 6.7, 20, 30 nmol/L Hg^{2+} respectively.

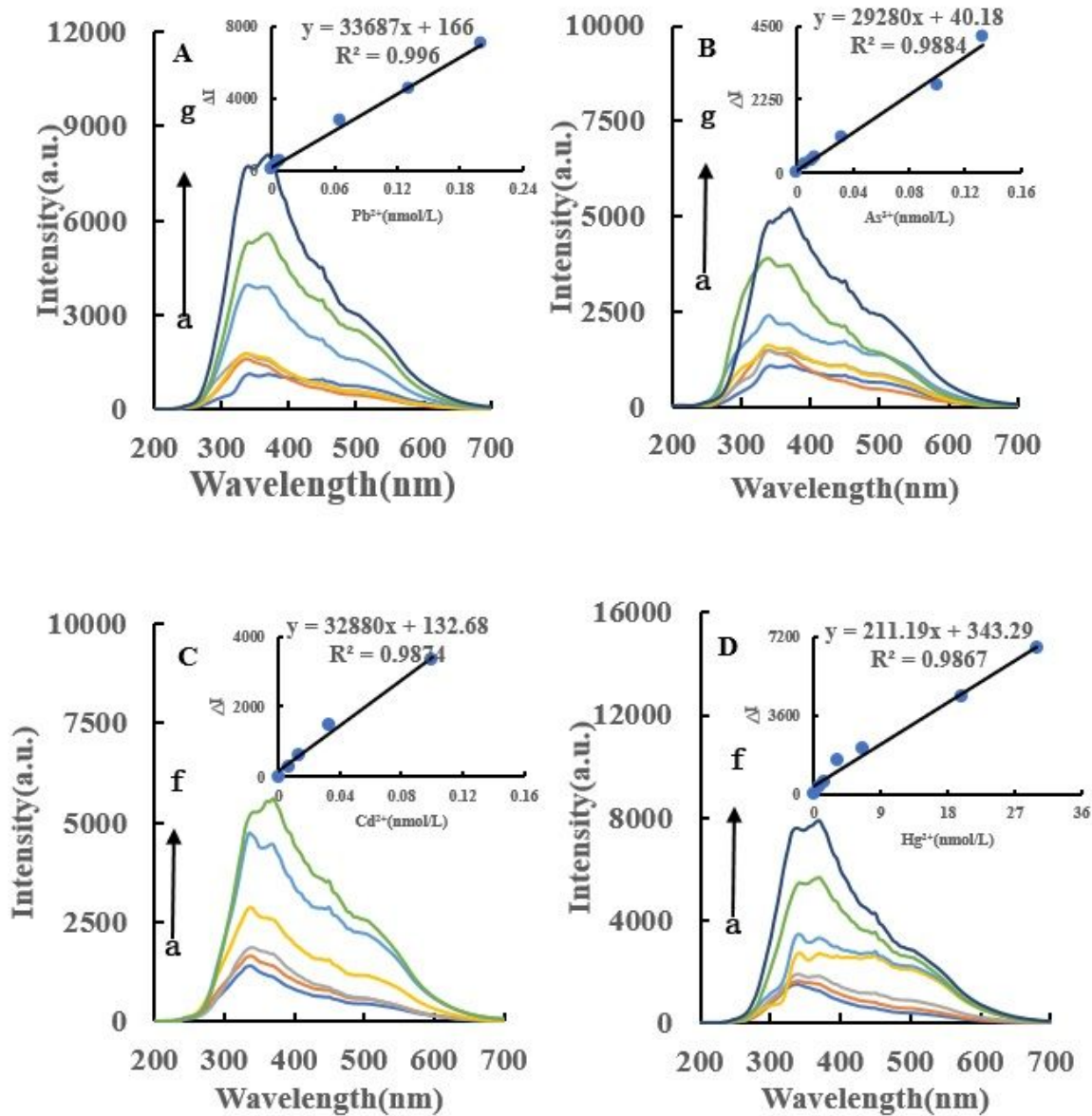


Figure 5

RRS spectra of $\text{CB@AgNPs} - \text{Fo} - \text{AgNO}_3 - \text{Apt}$ - inorganic pollutants system RRS spectrum system

A: Apt_{Pb}+NaAc-HAc+CB@AgNPs+AgNO₃+Fo, a to g represent 0, 4.47×10⁻³, 6.7×10⁻³, 8.94×10⁻³, 6.7×10⁻², 0.133 nmol/L Pb²⁺ and 0.201 nmol/L Pb²⁺ respectively. H: Apt_{As}+NaAc-HAc+CB@AgNPs +AgNO₃+Fo, a to g represent 0, 6.7×10⁻³, 1×10⁻², 1.33×10⁻², 3.3×10⁻², 0.1 and 0.133 nmol/L As³⁺ respectively. I: Apt_{Cd}+NaAc-HAc+ CB@AgNPs + AgNO₃+Fo, a to f represent 0, 6.7×10⁻³, 1.33×10⁻², 3.3×10⁻², 0.1 and 0.133 nmol/L Cd²⁺ respectively. J: Apt_{Hg}+NaAc-HAc+ CB@AgNPs +AgNO₃+Fo, a to g represent 0, 0.67, 1.33, 3.3, 6.7, 20, 30 nmol/L Hg²⁺ respectively.

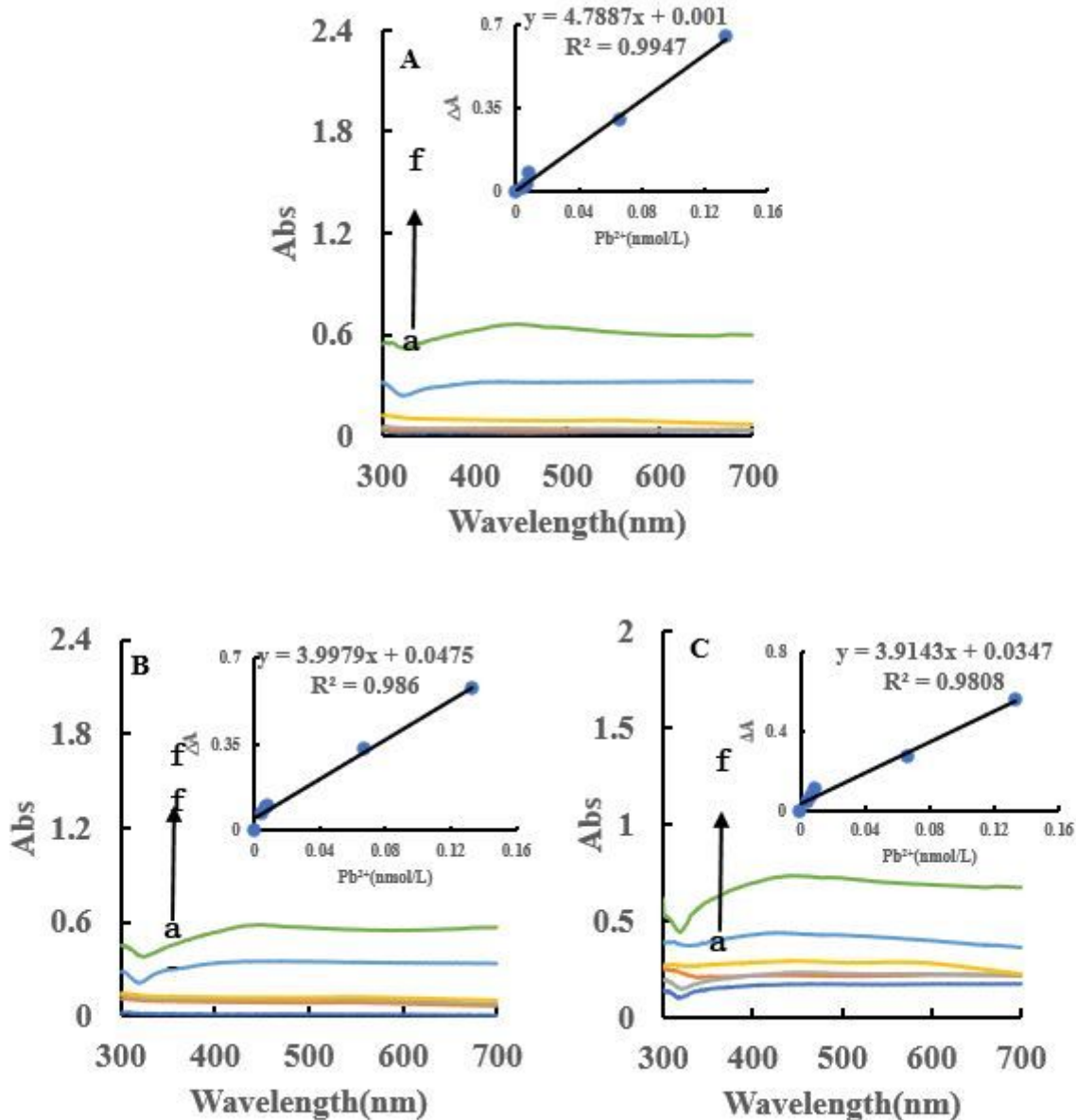


Figure 6

Abs spectra of Apt_{Pb}-CB@AgNPs -Fo-AgNO₃-Pb²⁺ system

Catalytic enhancement mechanism of LCs and CB@AgNPs on the AgNO₃-Fo nanoreaction.

Supplementary Files

This is a list of supplementary files associated with this preprint. Click to download.

- [SM.docx](#)